



City Research Online

City, University of London Institutional Repository

Citation: Wang, X., Yan, Y., Sun, Z. & Liu, C. (2014). LES investigation into the generation of momentum deficits in the supersonic wake of a micro-ramp. *Journal of Mechanical Science and Technology*, 28(4), pp. 1327-1337. doi: 10.1007/s12206-013-1164-x

This is the accepted version of the paper.

This version of the publication may differ from the final published version.

Permanent repository link: <https://openaccess.city.ac.uk/id/eprint/7378/>

Link to published version: <https://doi.org/10.1007/s12206-013-1164-x>

Copyright: City Research Online aims to make research outputs of City, University of London available to a wider audience. Copyright and Moral Rights remain with the author(s) and/or copyright holders. URLs from City Research Online may be freely distributed and linked to.

Reuse: Copies of full items can be used for personal research or study, educational, or not-for-profit purposes without prior permission or charge. Provided that the authors, title and full bibliographic details are credited, a hyperlink and/or URL is given for the original metadata page and the content is not changed in any way.

City Research Online:

<http://openaccess.city.ac.uk/>

publications@city.ac.uk

LES Investigation of the Generation of Momentum Deficit in the Supersonic Wake from a Micro-Ramp

Zhengzhong Sun¹, Yonghua Yan², Xiao Wang², Chaoqun Liu²

¹ Aerospace Engineering Department, Delft University of Technology, the Netherlands

² Math Department, University of Texas at Arlington, USA

Abstract

The implicitly implemented large eddy simulation (LES) with fifth order WENO scheme by solving the Navier-Stokes equations was carried out to explore the origin of the momentum deficit caused by a supersonic micro-ramp at flow conditions of $Ma=2.5$ and $Re_\theta=5760$. The numerical results were validated by qualitative and quantitative comparisons with existing experimental data. After describing the aerodynamic properties of the supersonic wake, such as the deficit and the streamwise vortices, the momentum deficit was later detected to originate from the lower portion of the upstream boundary layer while the high momentum fluid near the wall from the upper portion. The position alternation triggered by the micro-ramp was finally proposed as a revised mechanism.

1. Introduction

The micro-vortex generator (MVG), as a novel device for boundary layer control, has received interests in various aerodynamic applications^[1]. Among different types of MVGs^[2,3], the micro-ramp obtains a solid wedge shape and two slant side edges. The height of the micro-ramp is usually within 10%-50% of the boundary layer thickness as the definition in the review of Lin^[1]. The positive effects of the micro-ramp have been reported in the preceding researches. A typical application is intended for separation reduction produced in a shock wave/boundary layer interaction (SWBLI)^[2-8].

Although the effects have been demonstrated through the foregoing studies, the flow physics of the micro-ramp has not been fully understood due to the complex geometry of current device. Abundant efforts have been recently devoted to investigate the flow properties through both numerical^[9-12] and experimental^[13-14] methods. The major features including the momentum deficit and the primary vortex pair were originally visualized by Holden and Babinsky through wind tunnel experiments^[5]. These features were later confirmed qualitatively by the LES results of Lee and Loth^[2]. Benefited from the high order scheme which is able to resolve detailed turbulent structures, the LES study of Li et al.^[9] summarized several other flow features, such the ring vortex generated by the Kelvin-Helmholtz (K-H) instability at the circular shear layer. The momentum deficit and primary vortices were again validated qualitatively there^[9]. Since these two features are especially significant in the wake of the micro-ramp, a question would be raised regarding the connection between them: Is the momentum deficit a result of the primary vortices, or where is the origin of the low momentum fluid in the deficit region? Current numerical research is dedicated to answer the above questions. An existing knowledge of the deficit generation is based on the two dimensional visualization of the cross flow and considers that it is formed by lifting the low momentum fluid in the boundary layer through the streamwise trailing vortices. On the other hand, the high momentum fluid in the free stream is entrained into the near wall region. In this way, the exchange of fluids with different momentum is achieved. As a result, the downstream vortex pair is considered as the major role throughout the extension of streamwise wake. However, the LES study of Li et al.^[9] proposed another answer in a three dimensional point of view. In their study, the deficit region was traced to originate in the upstream turbulent boundary layer.

In order to consolidate the observation of Li et al.^[9], the flow around the micro-ramp was simulated by means of LES with high order high resolution difference scheme in the present study. In the following sections, the numerical algorithm and grid discretization are going to be explained firstly. Comparisons with experiment data are

later reported, such that the following discussions are based on a convincing ground. Prior the discussion of the deficit origin, the aerodynamic features of the wake region, especially the structure of the deficit region and properties of the vortices, are discussed in detail. In the exploration of the deficit origin, streamline tracing at several heights in the incoming boundary layer was performed. Later on, further investigations towards the velocity development along the intended streamlines were carried out. Some conclusions are finally arrived and a revised working mechanism of the micro-ramp is then proposed.

2. Numerical Algorithm

The current simulation of the micro-ramp flow was carried out by solving the unfiltered form of the Navier-Stokes (N-S) equations. Without explicitly implementing subgrid scale models, the current method uses the intrinsic dissipation of the numerical algorithm to dissipate the turbulent energy accumulated at the unresolved scales with high wave numbers. It is hence referred to be the implicitly implemented LES.

2.1 Governing Equations

The nondimensional Navier-Stokes equations in conservation form are considered as the governing equations and written in a general form as eq.(1).

$$\frac{\partial Q}{\partial t} + \frac{\partial E}{\partial x} + \frac{\partial F}{\partial y} + \frac{\partial G}{\partial z} = \frac{\partial E_v}{\partial x} + \frac{\partial F_v}{\partial y} + \frac{\partial G_v}{\partial z} \quad (1)$$

where

$$Q = \begin{pmatrix} \rho \\ \rho u \\ \rho v \\ \rho w \\ e \end{pmatrix}, \quad E = \begin{pmatrix} \rho u \\ \rho u^2 + p \\ \rho uv \\ \rho uw \\ (e+p)u \end{pmatrix}, \quad F = \begin{pmatrix} \rho v \\ \rho vu \\ \rho v^2 + p \\ \rho vw \\ (e+p)v \end{pmatrix}, \quad G = \begin{pmatrix} \rho w \\ \rho wu \\ \rho wv \\ \rho w^2 + p \\ (e+p)w \end{pmatrix},$$

$$E_v = \frac{1}{\text{Re}} \begin{pmatrix} 0 \\ \tau_{xx} \\ \tau_{xy} \\ \tau_{xz} \\ u\tau_{xx} + v\tau_{xy} + w\tau_{xz} + q_x \end{pmatrix}, \quad F_v = \frac{1}{\text{Re}} \begin{pmatrix} 0 \\ \tau_{yx} \\ \tau_{yy} \\ \tau_{yz} \\ u\tau_{yx} + v\tau_{yy} + w\tau_{yz} + q_y \end{pmatrix}, \quad G_v = \frac{1}{\text{Re}} \begin{pmatrix} 0 \\ \tau_{zx} \\ \tau_{zy} \\ \tau_{zz} \\ u\tau_{zx} + v\tau_{zy} + w\tau_{zz} + q_z \end{pmatrix},$$

$$e = \frac{p}{\gamma-1} + \frac{1}{2} \rho (u^2 + v^2 + w^2),$$

$$q_x = \frac{\mu}{(\gamma-1)Ma_\infty^2 \text{Pr}} \frac{\partial T}{\partial x}, \quad q_y = \frac{\mu}{(\gamma-1)Ma_\infty^2 \text{Pr}} \frac{\partial T}{\partial y}, \quad q_z = \frac{\mu}{(\gamma-1)Ma_\infty^2 \text{Pr}} \frac{\partial T}{\partial z},$$

$$p = \frac{1}{\gamma Ma_\infty^2} \rho T, \quad Pr=0.72,$$

$$\tau = \mu \begin{pmatrix} \frac{4}{3} \frac{\partial u}{\partial x} - \frac{2}{3} \left(\frac{\partial v}{\partial y} + \frac{\partial w}{\partial z} \right) & \frac{\partial u}{\partial y} + \frac{\partial v}{\partial x} & \frac{\partial u}{\partial z} + \frac{\partial w}{\partial x} \\ \frac{\partial u}{\partial y} + \frac{\partial v}{\partial x} & \frac{4}{3} \frac{\partial v}{\partial y} - \frac{2}{3} \left(\frac{\partial w}{\partial z} + \frac{\partial u}{\partial x} \right) & \frac{\partial v}{\partial z} + \frac{\partial w}{\partial y} \\ \frac{\partial u}{\partial z} + \frac{\partial w}{\partial x} & \frac{\partial v}{\partial z} + \frac{\partial w}{\partial y} & \frac{4}{3} \frac{\partial w}{\partial z} - \frac{2}{3} \left(\frac{\partial u}{\partial x} + \frac{\partial v}{\partial y} \right) \end{pmatrix}.$$

The viscous coefficient is approximated by Sutherland's law

$$\mu = T^{\frac{3}{2}} \left(\frac{1+S}{T+S} \right), \quad (2)$$

where S is Sutherland constant and $S = 110.4/T_\infty$.

As the governing equations are described in the nondimensional form in eq.(1). The variables are nondimensionalized in the following way:

$$\begin{aligned} x &= \frac{\tilde{x}}{L}, \quad y = \frac{\tilde{y}}{L}, \quad z = \frac{\tilde{z}}{L}, \\ u &= \frac{\tilde{u}}{U_\infty}, \quad v = \frac{\tilde{v}}{U_\infty}, \quad w = \frac{\tilde{w}}{U_\infty}, \\ \mu &= \frac{\tilde{\mu}}{\mu_\infty}, \quad k = \frac{\tilde{k}}{k_\infty}, \quad \rho = \frac{\tilde{\rho}}{\rho_\infty}, \quad p = \frac{\tilde{p}}{\rho_\infty U_\infty^2}, \quad e = \frac{\tilde{e}}{\rho_\infty U_\infty^2}, \end{aligned}$$

where the variables with tilde are the dimensional counterparts.

As the calculation was performed in the computational domain containing an arbitrary orthogonal curvilinear coordinates, the physical domain is transformed in the following way:

$$\begin{cases} \xi = \xi(x, y, z) \\ \eta = \eta(x, y, z) \\ \zeta = \zeta(x, y, z) \end{cases} \quad (3)$$

As a result, the governing equations should be rewritten as eq.(4) using the arbitrary orthogonal curvilinear coordinates

$$\frac{\partial \hat{Q}}{\partial \tau} + \frac{\partial \hat{E}}{\partial \xi} + \frac{\partial \hat{F}}{\partial \eta} + \frac{\partial \hat{G}}{\partial \zeta} = \frac{\partial \hat{E}_v}{\partial \xi} + \frac{\partial \hat{F}_v}{\partial \eta} + \frac{\partial \hat{G}_v}{\partial \zeta} \quad (4)$$

where

$$\begin{aligned} \hat{Q} &= J^{-1} Q \\ \hat{E} &= J^{-1} (\xi_x E + \xi_y F + \xi_z G), \quad \hat{F} = J^{-1} (\eta_x E + \eta_y F + \eta_z G), \quad \hat{G} = J^{-1} (\zeta_x E + \zeta_y F + \zeta_z G), \\ \hat{E}_v &= J^{-1} (\xi_x E_v + \xi_y F_v + \xi_z G_v), \quad \hat{F}_v = J^{-1} (\eta_x E_v + \eta_y F_v + \eta_z G_v), \quad \hat{G}_v = J^{-1} (\zeta_x E_v + \zeta_y F_v + \zeta_z G_v). \end{aligned}$$

2.2 Finite difference schemes

(1) Fifth-order WENO scheme for the convective terms

The fifth-order WENO scheme was chosen to discrete the convective terms. For clarity, its implementation is explained through the one-dimensional hyperbolic equation, eq.(5).

$$\frac{\partial u}{\partial t} + \frac{\partial f(u)}{\partial x} = 0 \quad (5)$$

The semi-discretization of eq.(5) can be written as eq.(6):

$$\left(\frac{\partial u}{\partial t} \right)_j = - \frac{h_{j+\frac{1}{2}} - h_{j-\frac{1}{2}}}{\Delta x} \quad (6)$$

Considering the positive flux, the three upwind-biased schemes on three basic candidate stencils are given as eq.(7):

$$\begin{cases} h_1^{+} = \frac{1}{3} f_{j-2} - \frac{7}{6} f_{j-1} + \frac{11}{6} f_j \\ h_2^{+} = -\frac{1}{6} f_{j-1} + \frac{1}{3} f_j + \frac{5}{6} f_{j+1} \\ h_3^{+} = \frac{1}{3} f_j + \frac{5}{6} f_{j+1} - \frac{1}{6} f_{j+2} \end{cases} \quad (7)$$

where the superscript “+” refers to the positive flux after flux splitting. The final nonlinear weighted scheme can be written as eq.(8)

$$h_{j+\frac{1}{2}}^{+} = w_1 h_1^{+} + w_2 h_2^{+} + w_3 h_3^{+} \quad (8)$$

where $w_i = b_i / \sum_{i=1}^3 b_i$, $b_i = \alpha_i / (\varepsilon + IS_i)^2$, $(\alpha_1, \alpha_2, \alpha_3) = (0.1, 0.6, 0.3)$. It should be noted that ε is a small quantity to prevent the denominator from being zero, and should obtain a small number in the supersonic problems containing shock waves ($10^{-6} \square 10^{-10}$). IS_i is the smoothness measurement and has the form of eq.(9)

$$\begin{cases} IS_1 = \frac{13}{12}(f_{j-2} - 2f_{j-1} + f_j)^2 + \frac{1}{4}(f_{j-2} - 4f_{j-1} + 3f_j)^2 \\ IS_2 = \frac{13}{12}(f_{j-1} - 2f_j + f_{j+1})^2 + \frac{1}{4}(f_{j-1} - f_{j+1})^2 \\ IS_3 = \frac{13}{12}(f_j - 2f_{j+1} + f_{j+2})^2 + \frac{1}{4}(3f_j - 4f_{j+1} + f_{j+2})^2 \end{cases} \quad (9)$$

The expression for $h_{j+\frac{1}{2}}^-$ has the symmetric form of $h_{j+\frac{1}{2}}^+$ with respect to the point of $x_{j+\frac{1}{2}}$.

(2) Finite difference scheme for the viscous terms

The standard central difference scheme was applied to discrete the second order viscous terms on the right-hand side of eq.(4).

(3) The temporal scheme

The explicit third-order TVD-type Runge-Kutta scheme was applied for temporal discretization. The scheme was implemented using eq.(10)

$$\begin{cases} u^{(1)} = u^n + \Delta t \cdot L(u^n) \\ u^{(2)} = \frac{3}{4}u^n + \frac{1}{4}u^{(1)} + \frac{1}{4}\Delta t \cdot L(u^{(1)}) \\ u^{n+1} = \frac{1}{3}u^n + \frac{2}{3}u^{(2)} + \frac{2}{3}\Delta t \cdot L(u^{(2)}) \end{cases} \quad (10)$$

2.3 Boundary conditions

(1) Inflow condition

In order to guarantee a fully developed turbulent flow, the inflow condition were treated with two parts, the mean component and the fluctuation component. The averaged boundary layer profile from the DNS result^[15] was implemented into current grid system through third-order spline interpolation. The transplant was carried out by assuming the non-dimensional velocity (u/U_∞) scales with (y/δ^*).

The temperature profile at inlet was determined by eq.(11),

$$\frac{T}{T_\infty} = \frac{T_w}{T_\infty} - \frac{r}{2}(\gamma - 1)Ma_\infty^2 \left(\frac{u}{U_\infty} \right)^2 \quad (11)$$

where r is the recovery factor with value $r=0.9$ and the adiabatic wall temperature was determined by eq.(12),

$$\frac{T_w}{T_\infty} = 1 + \frac{r}{2}(\gamma - 1)Ma_\infty^2 \quad (12)$$

Pressure p was set uniform at inlet and density ρ was calculated by eq.(13)

$$\rho = \frac{p}{RT} \quad (13)$$

Fluctuation components of velocity were also acquired from DNS^[15] and form an input dataset of 20,000 fluctuation profiles. They were later added into the averaged profile according to different time steps. By performing derivative to eq.(11), the temperature fluctuation can be approximated through eq.(14)

$$\frac{\Delta T}{T_\infty} = -r(\gamma - 1)Ma_\infty^2 \frac{u}{U_\infty} \Delta u \quad (14)$$

The density fluctuation was then calculated by eq.(15)

$$\frac{\Delta\rho}{\rho_\infty} = \frac{\Delta T}{T_\infty} \quad (15)$$

The mean data and the fluctuation data were finally summed up and implemented as the inlet boundary condition

(2) Boundary conditions for the four sides

Non-slip condition was applied to the flow floor, where adiabatic and zero-gradient of pressure were also used. They are expressed in eq.(16)-(18)

$$\bar{u} = 0 \quad (16)$$

$$\frac{\partial T}{\partial n} = 0 \quad (17)$$

$$\frac{\partial p}{\partial n} = 0 \quad (18)$$

Periodic boundary conditions were implemented to the side walls, and the upper boundary was treated as the free stream, and the free stream variables were applied there.

3. Case Description and Grid Generation

3.1 Case description

The free stream Mach number was $Ma=2.5$. The height of the micro-ramp was chosen at $h=3$ mm. A declining angle of 70 degrees was applied to the geometry. The width and chord length of the device were $w=5.857h$ and $c=6.942h$, respectively. The geometry of the present micro-ramp is plotted in figure 1.

The boundary layer was measured to obtain a thickness of $2.32h$ in the immediate front of the micro-ramp after development of approximately $11.52h$. A ratio of $h/\delta_{99}=0.431$ was achieved, which means the micro-ramp was deeply immersed inside the boundary layer. The displacement thickness of the undisturbed boundary layer was $\delta^*=0.323h$, and the momentum thickness was $\theta=0.229h$. The shape factor is then determined to be $H=1.407$. The flow information of the undisturbed boundary layer is summarized in table 1.

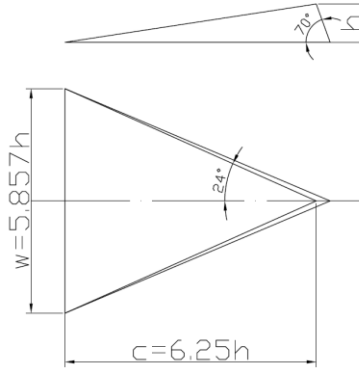


Fig. 1. The dimensions of the micro-ramp.

Parameter	Quantity
Ma_∞	2.5
δ_{99}/h	2.322
δ^*/h	0.323
θ/h	0.229
H_{inc}	1.407
u_τ/u_∞	0.0552
Re_θ	5760

Table 1. The simulation condition and undisturbed boundary layer parameters.

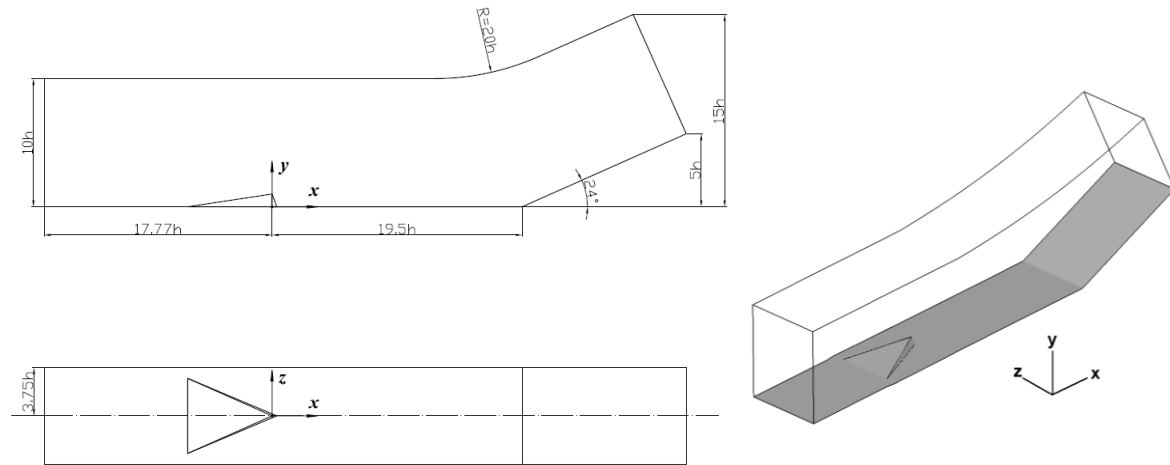
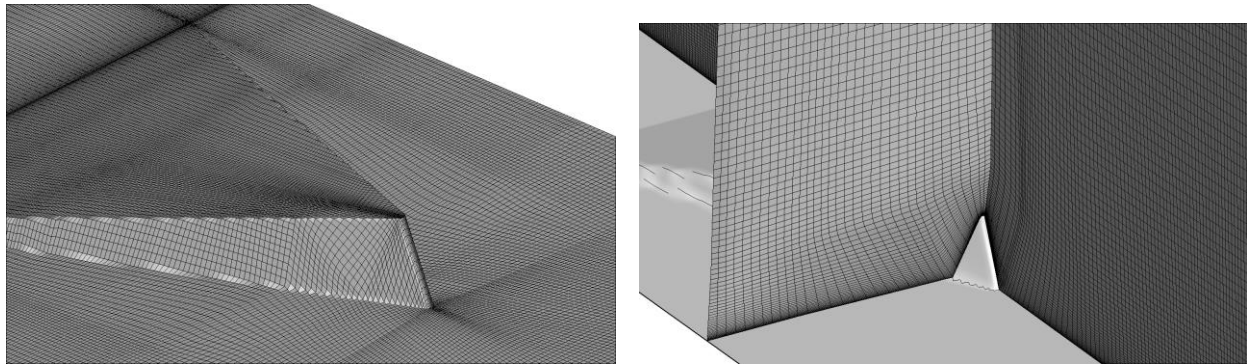


Fig. 2. The computational domain.

3.2 Grid discretization

In order to maintain clarity and simplicity, a single micro-ramp was installed. The computational domain is depicted in figure 2. It should be noted that a 24° raising ramp was installed downstream for the SWBLI research. Since SWBLI is not relevant to the current topic, the flow physics happened there is not going to be reported. The origin of the coordinate system is placed on the point where the apex of micro-ramp is projected onto the floor, while x -axis is in the downstream direction, y -axis in wall normal direction and z -axis in spanwise direction. Current coordinate system is consistent with the existing literatures, so that comparisons can be made after proper scaling. Throughout the paper, the distance is scaled with the micro-ramp height h , while the velocity is scaled with the free stream velocity U_∞ .

The whole domain has a streamwise extension of $50.07h$. The inlet is located at $x/h=-17.77$. The floor behind the micro-ramp remains flat for a length of $19.5h$. The half width of the domain is $3.75h$ and the height extends from $10h$ to $15h$. The flow domain was divided into five sections, namely the inlet region, MVG region, ramp region and two transition regions adjacent the MVG region, to guarantee proper transition of the grid system. Body-fitted methodology was applied to the flow domain, especially the MVG region, so that proper orthogonality is ascertained. The steps to generate the current grid system are given in detail in ref.[8]. The grid distributions on and around the micro-ramp are plotted in figure 3, respectively. The first grid point off the wall is arranged at $y/h=0.00322$ and approximately 120 grid points in wall normal direction were used to resolve the turbulent boundary layer. The grid number for the entire system is resulted to be $n_x \times n_y \times n_z = 1600 \times 190 \times 128$.



(a) Surface mesh on the micro-ramp;

(b) Mesh surrounding the micro-ramp

Fig. 3. The optimized grid system surrounding the micro-ramp.

4. Results Validation

Code validation has already been carried out through the supersonic flow around a half cylinder and a delta wing^[8,16], where the difference scheme and boundary treatment are testified. The present section mainly focuses on the comparison between current numerical results and experimental data.

4.1 The undisturbed turbulent boundary layer

The averaged undisturbed turbulent boundary layer in the immediate front of the micro-ramp is nondimensionalized and plotted in figure 4. The profile from the PIV measurement of Sun et al.^[14] is also included. Overlap is well for the upper part ($y/\delta > 0.4$) of the two profiles. Discrepancy can be observed for the lower portions, where the computation produced a profile less full than the experimental data.

Current boundary layer profile is also plotted in wall unit in figure 5. The fitted profile complies with the log-law in the region approximately from $30 < y^+ < 100$, which is shorter than the typical value, where the log region goes up to $y^+ = 300$. As a result a larger wake component is generated. On the other end, the current result resolves the linear region till $y^+ = 0.38$

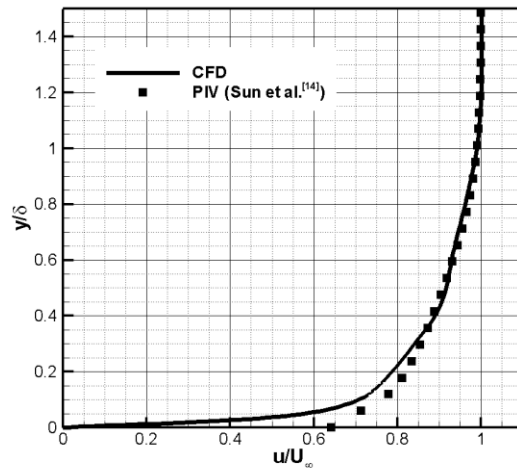


Fig. 4. The undisturbed turbulent boundary layer.

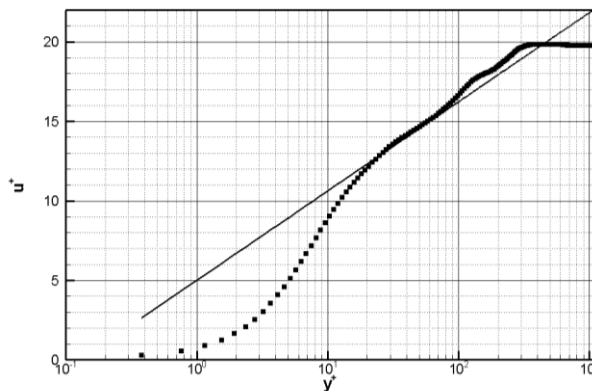
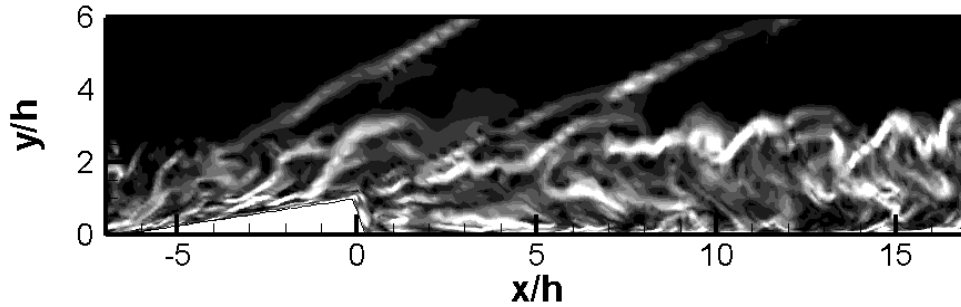


Fig. 5. The undisturbed turbulent boundary layer profile in wall unit.

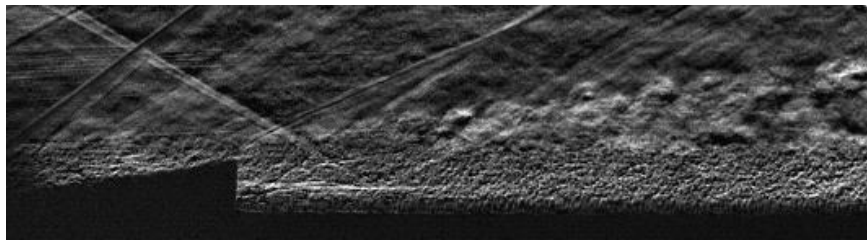
4.2 Flow visualization

A snapshot of numerical schlieren image is displaced in figure 6(a) through the gradient of the density ($\nabla \rho$) at the center plane ($z/h=0$). Two shock waves emanating from the micro-ramp are resolved. In figure 6(b), a

schlieren image from the wind tunnel experiment of Rogier^[17] is presented. The angle of the leading shock in figure 6(b) is larger in the experiment, as the flow condition is different, where the flow ran at $Ma=2.0$ and the ratio of $h/\delta=0.67$. Apart from the two shock waves, the roller structures identified as the Kelvin-Helmholtz instability of the shear layer is also resolved at the interface of the wake region and free stream.



(a) Numerical instantaneous schlieren image

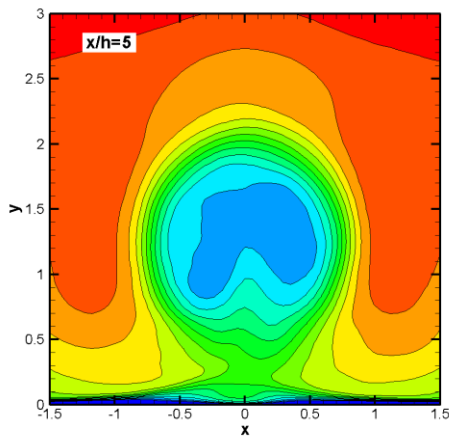


(b) Experimental schlieren snapshot

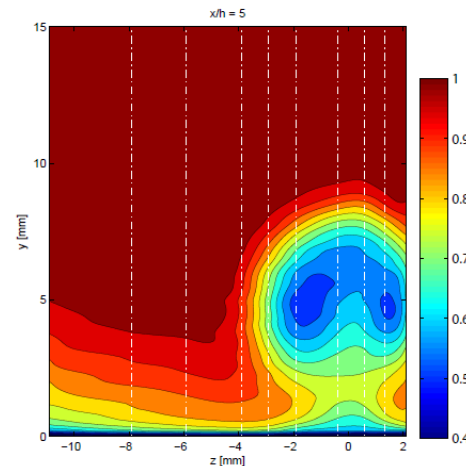
Fig. 6. Flow visualization at the center plane ($z/h=0$)

4.3 The cross flow structure

A cross flow section at $x/h=5$ is extracted from the averaged flow field, so that qualitative comparison with the LDV measurement of Oorebeek et al.^[18] can be made. In the u -contour in figure 7(a), the momentum deficit is clearly resolved. The width and height of current deficit region are approximately $2h$ and $2.2h$ respectively, while they are roughly $2h$ and $2.25h$ in figure 7(b). However, the two cores of low- u as measured by LDV are not resolved through computation. The contours of v are compared in figure 8. Both the upwash and downwash events are revealed by current computation, but are estimated with weaker strength. A sharp eye would detect a small region of negative v below the central upwash. Such a region is also measured in the experiment^[18].

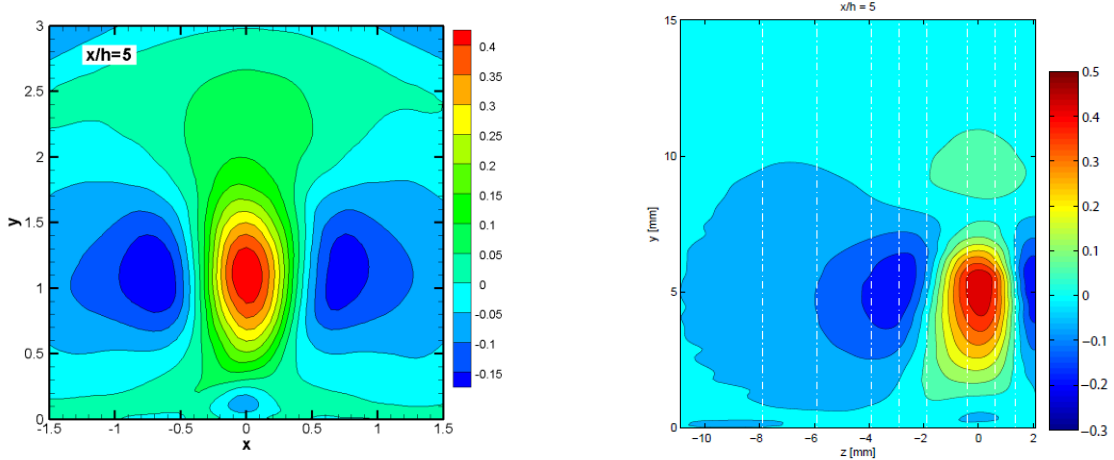


(a) Current LES result;



(b) LDV measurement of Oorebeek et al.^[18]

Fig. 7. Contours of averaged u at $x/h=5$.

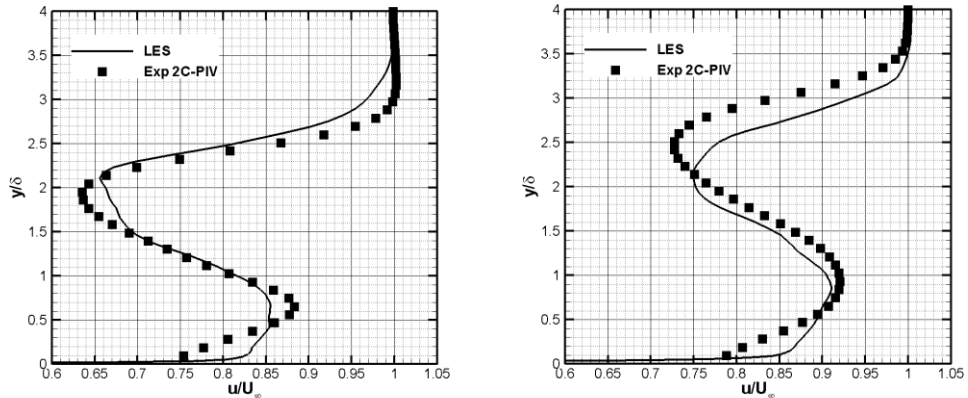


(a) Current LES result; (b) LDV measurement of Oorebeek et al.^[15]
 Fig. 8. Contours of averaged v at $x/h=5$.

4.4 The velocity profile in the wake region

The velocity profiles of u at $x/h=10$ and 15 at the central plane ($z/h=0$) are quantitatively compared with the PIV measurement of Sun et al.^[14] in figure 9. At the upstream position of $x/h=10$, the LES data follows well with the measurement, especially the shear region above and below the deficit. But the deficit is slightly underestimated. Discrepancy can be observed at the downstream position of $x/h=15$, and an underestimated deficit is also approximated by LES.

As no identical experimental conditions (such as Mach number, Reynolds number etc.) as current LES research are available, deviations of both sets of results can be expected. Since great similarity has been revealed through the comparison in this section, confidence of the resultant validity can then be placed on the current numerical results.



(a) $x/h=10$ (b) $x/h=15$
 Fig. 9. The profiles of averaged u at the center plane ($z/h=0$)

5. The Momentum Deficit

5.1 The deficit in the mean flow

As an entry to the understanding of the momentum deficit generation, the mean and instantaneous flow properties of the supersonic wake that contains the momentum deficit are first introduced. An overall view of the

averaged wake is plotted in figure 10, where three different streamwise slices of u and v contours are included, so that the streamwise development can be visualized. It should be mentioned that the color bar for u is chosen from $0.4U_\infty$ to $1.0U_\infty$, instead of starting from 0, for better visualization of the decayed flow pattern further downstream. A region with significant low u is produced immediately after the micro-ramp. Elevation in position and recovery in magnitude are experienced when traveling downstream. Correspondingly, the v forms a focused central upwash and two symmetric downwash events at both sides, which coalesce to notify the counter rotating vortex pair. The decay of v -event also happens throughout the development. A sharp reader would notice the wavy contour lines close to the flow floor in figure 10(a). This is the residual large structure embedded in the turbulent boundary layer from the DNS result, as limited ensemble size ($N=300$) is used for averaging the flow.

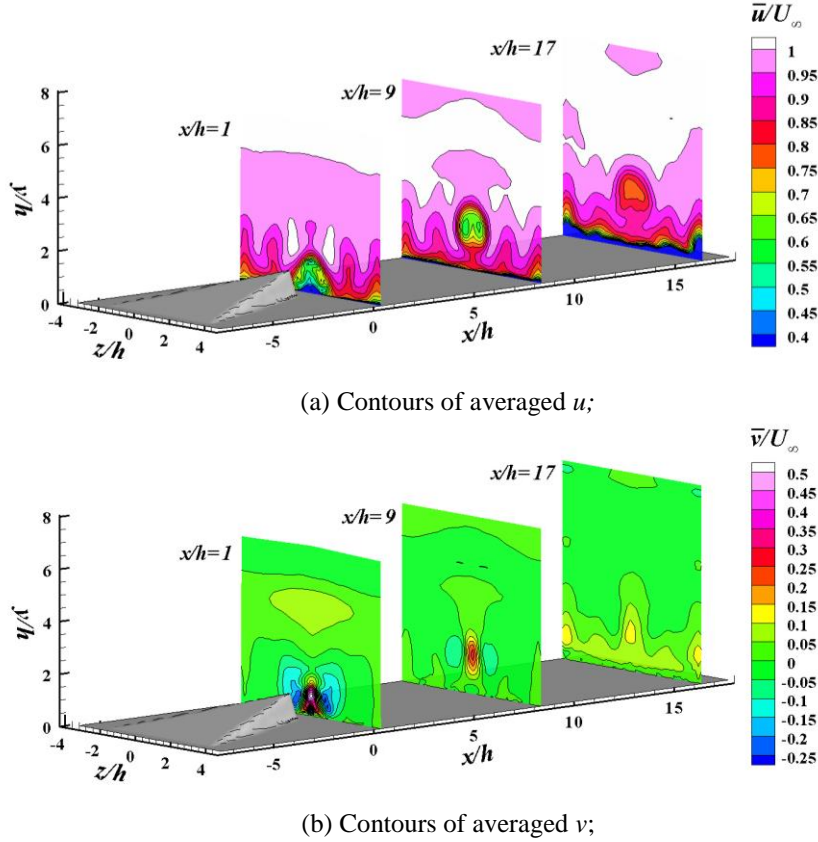


Fig. 10. An overview of the streamwise development of the micro-ramp wake, cross-sections are at $x/h=1, 9$ and 17 respectively.

In order to investigate the wake in detail, the three cross-sections in figure 10 are further enlarged in figure 11. The color bars are kept consistent with those in figure 10. The intended momentum deficit can be easily detected through the region containing weak u . A triangular shape is displayed at $x/h=1$ as it is the initial stage of the deficit. Upon leaving the wall, a circular shape as shown in figure 11(b) is obtained. Throughout the development of the wake, the minimum u decreases from $0.5U_\infty$ at $x/h=1$ to $0.8U_\infty$ at $x/h=17$. Due to the velocity difference between the free stream and the deficit, a shear layer is formed wrapping the deficit.

As the presence of the symmetric slant edges of the micro-ramp, a pair of opposing vortices is produced in streamwise direction. These two vortices can be observed through the overlaid vectors and they are located inside the deficit region. The vortices also decay, as strong swirling vectors are visualized at $x/h=1$ while they are barely visible at $x/h=17$.

The focused central upward region of v is generated as a joint result of upwash vectors. Meanwhile, two symmetric downwash events are produced, obtaining approximately half the strength of the upwash in measure of v magnitude. Following the decay of vorticity strength, the maximum upward v of $0.5U_\infty$ at $x/h=1$ reduces to approximately $0.1U_\infty$ at $x/h=17$, indicating a weak imprint of upwash in the downstream position.

A side observation of the vectors in figure 11(a) and 11(d) features the secondary vortex pair shedded from the root portion of the sharp trailing edge. This pair of secondary vortices also obtain counter rotations and are

produced in a smaller scale than the primary pair. Since it is not very influential to the present topic of the large scale momentum deficit, this secondary pair is not going to be elaborated in detail.

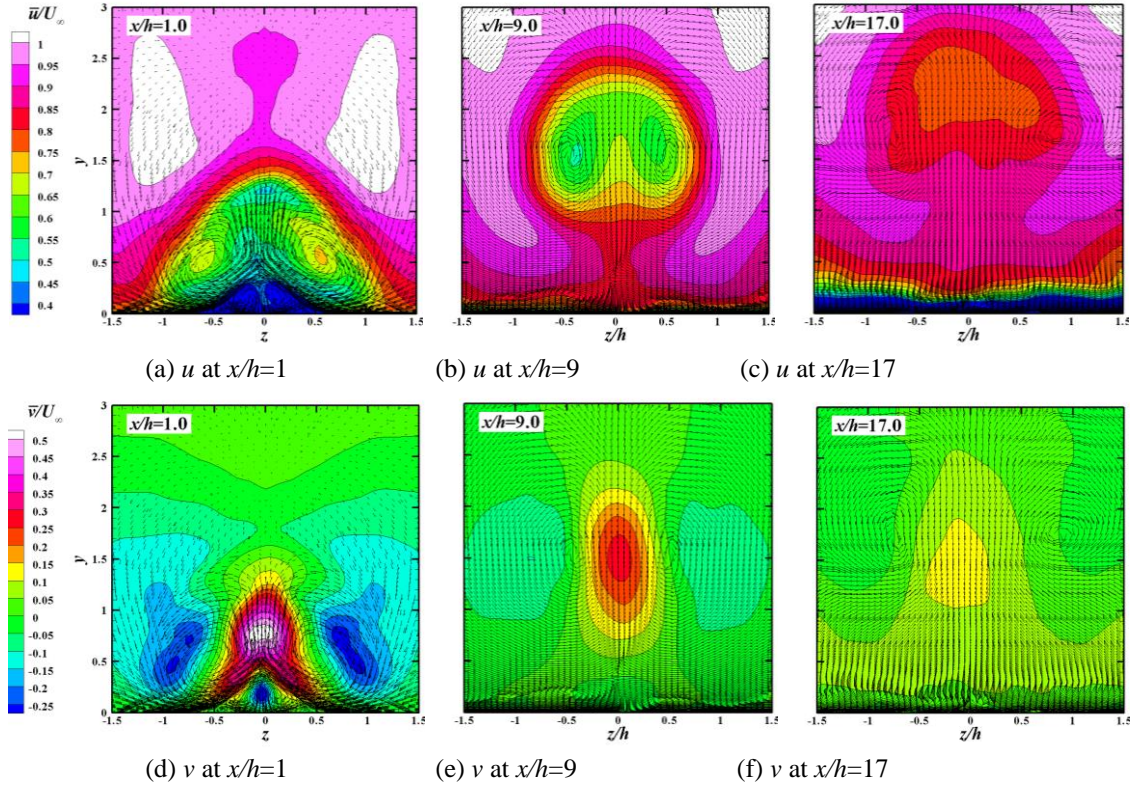


Fig. 11 Cross-sections of mean u and v contours at three streamwise positions with two-dimensional vectors overlaid.

5.2 The deficit in the instantaneous flow

Instead of visualizing the smoothed flow patterns through averaged flow field, the instantaneous realizations on the other hand offer to exhibit the instantaneous variations. Cross-sections at $x/h=1, 9$ and 17 are again extracted from one flow field snapshot and plotted in figure 12.

All the revealed structures, such as the u -deficit, the upwash and downwash, and the primary vortex pair, can also be observed in the instantaneous velocity contours. At the immediate downstream of the trailing edge, i.e. $x/h=1.0$, the contours of both u and v resemble the averaged pattern with only a slight curvature of the contour lines, indicating greater flow instability. Further downstream, considerable variations are presented. For the current instantaneous representation at $x/h=9$, the mushroom-shaped u -deficit has sever curved edges and it further inclined towards the left side at $x/h=17$. The upward region of v at $x/h=9$ obtains a central peak magnitude of approximately $0.3U_\infty$, however a stronger downwash with $v=-0.2U_\infty$ at the right side is generated, suggesting the asymmetric vortex strength. Although a peak of upward v still persists at $x/h=17$, it only survives in a really small region with $v=0.25U_\infty$ and deviates from the central location.

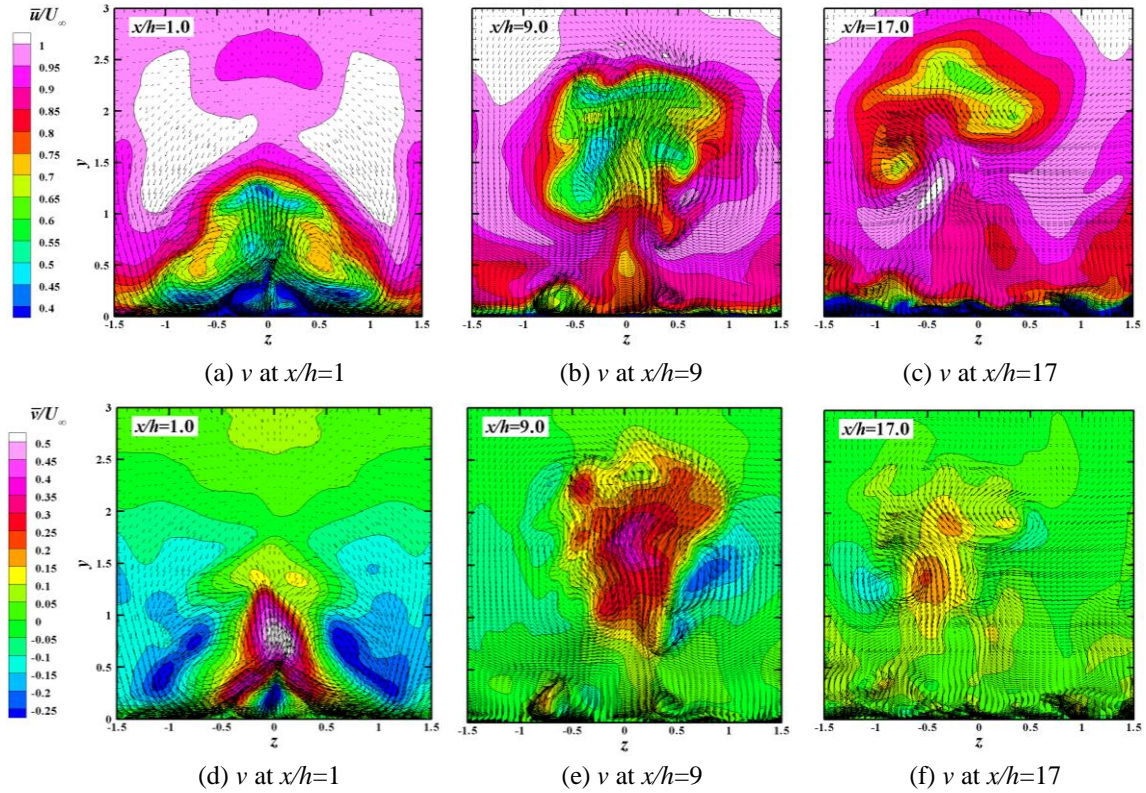


Fig. 12 Cross-sections of instantaneous u and v contours at three streamwise positions with two-dimensional vectors overlaid.

5.3 The mean and instantaneous streamwise vortical structure

Although the streamwise vortices can be observed and qualitatively studied from the overlaid vectors in the contour plots, a dedicated representation and quantitative investigation can be achieved through the distribution of streamwise vorticity component as plotted in figure 13. It should be mentioned that the instantaneous vorticity in the right column is calculated from the same snapshot in figure 3, and different color bars are used for the purpose of visualizing the reduced magnitude of downstream vorticity. Decent symmetry of the vortex pair is presented through the mean representation, although curved edges can be observed due to limited statistical ensemble size. Instead of using upward and downward v as an indication of vortical activity, a straightforward evaluation of the vorticity development can be achieved. The vortical strength at $x/h=17$ reduces to approximately one tenth of that at $x/h=1$.

Variation from the mean vortical pattern is exhibit by the instantaneous representations in the right column of figure 13. The primary vortex pair is produced on either side of the center plane, resembling the mean flow. Affected by fluctuation and flow instability, namely the Kelvin-Helmholtz instability (see Sun et al.^[14]), the focused mean vorticity pattern is distributed into several irregular spatial pockets following the variation of the u -deficit.

The mommtum deficit can so far be understood as a region containing reduced magnitude of u with a central upwash and side downwashes. On the other hand, a pair of primary opposing vortices is generated and obtains a similar decay process as the velocity patterns.

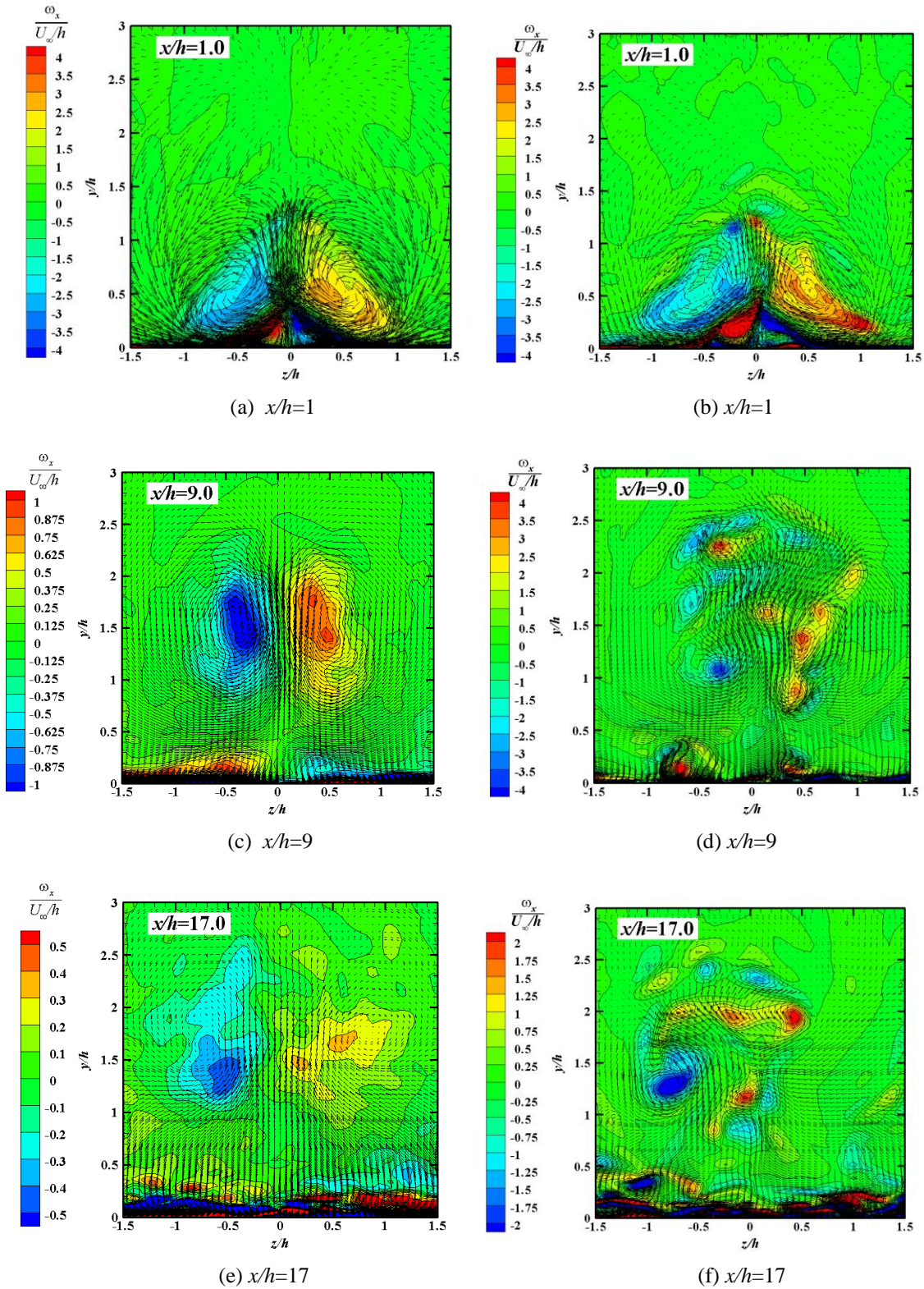


Fig. 13 Cross-sectional contours of streamwise component of vorticity ω_x .

6. The Origin of Momentum Deficit

In order to reveal the source of momentum deficit, streamline tracing at different wall-normal positions are carried out and six of them are plotted in figure 14. This analysis is based on the mean flow field. Figure 14(a) shows the streamlines that stem from $y_0/h=0.0092$. They mainly form the leading edge separation due to their low momentum. However, the streamlines close to the edges of the micro-ramp are capable of passing downstream and then contracted towards the center along the slant edges and are further lifted upward through the spiral motion. The flow outside the width of the micro-ramp is barely affected by the micro-ramp although slight curvature of the streamlines can be observed there. In figure 14(b), the streamlines originate from $y_0/h=0.0412$. The leading edge separation is reduced because of higher momentum the fluid obtains. More streamlines are entrained downstream by vortical motion and contribute into the u -deficit. As the tracing position is elevated, as shown in figure 14(c) and 14(d), no separation remains. The flow there along the whole span moves forward and concentrate into two parallel neighboring vortices through the spiral activity once the micro-ramp is past. However, less spiral motion is behaved by the flow originates from even higher wall-normal positions (as shown in figure 14(e) and 14(f)). The major portion of the flow along the micro-ramp span is directed downward and enters into the flow below the momentum-deficit, although a few streamlines close to the center are diverted outward forming the streamlines that wrap the deficit region and resultantly contribute to the circular shear layer.

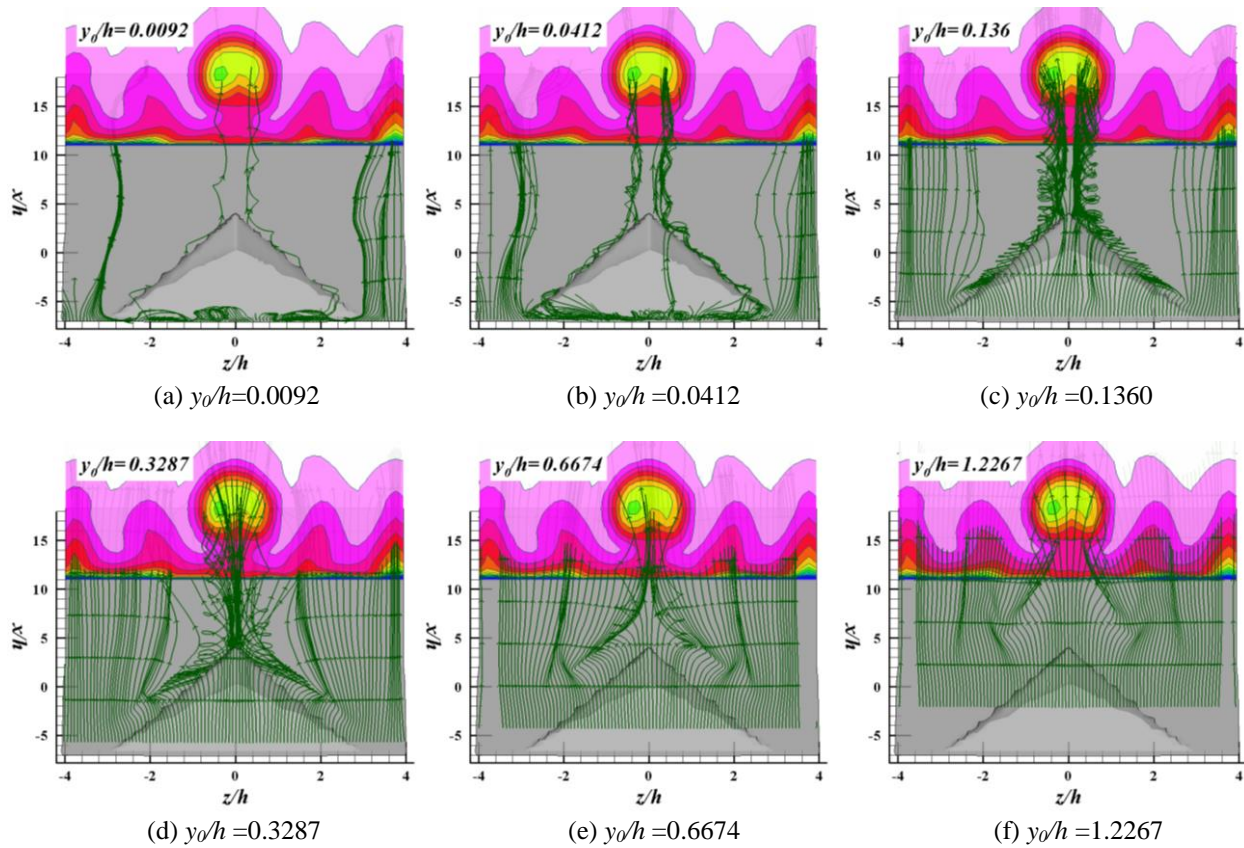


Fig. 14 Streamlines with origins at different wall-normal positions upstream of the micro-ramp.

The streamline rake originating from a fixed spanwise position at $z/h=1.1$ is further plotted in figure 15 to consolidate the above observations in figure 14. Apart from the confirmation of deficit origin from the lower portion of the boundary layer, the *position alternation* is better revealed: the lower level flow in the incoming boundary layer is lifted upward through the vortical activity forming the momentum deficit, while the upper level flow with higher momentum is, on the contrary, directed into a lower position past the micro-ramp, resulting in a fuller boundary layer close to the floor.

As the position alternation happens along the whole span of the micro-ramp, in order to entrain larger amount high momentum fluid of the incoming boundary layer into the near wall region, a wider micro-ramp should

be considered. Recall the result of Lee and Loth^[2], the half width micro-ramp produces worse downstream boundary layer than the regular type in measure of shape factor.

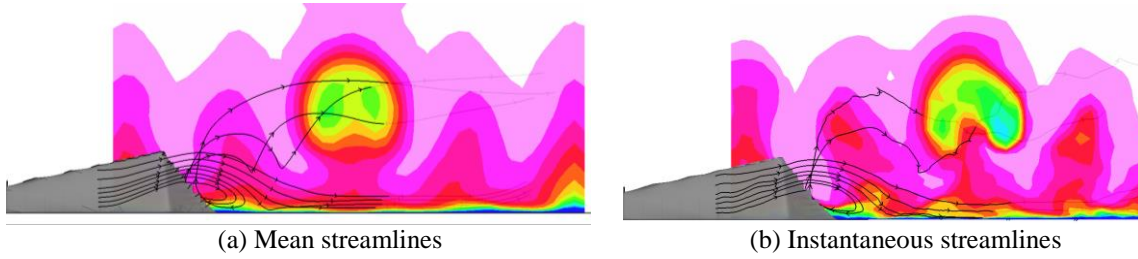


Fig. 15. Streamlines with origins at a fixed spanwise position $z/h=1.1$.

7. The Position Alternation – A Revised Mechanism

As revealed by section 6, the process of position alternation is going to be explored in detail. The seven mean streamlines in figure 15(a) are extracted and projected into the x - y plane as shown in figure 16. It should be mentioned that the axis ratio is exaggerated to help observation. It should also be noted that no line map is listed in figure 16 as they can be identified from the position of origination. Solid lines are used to feature the lower level streamlines which are lifted, while dashed lines for the higher level flow entrained downward. The same line system is applied to figure 17. A clear bifurcation of the streamlines right after the micro-ramp is better visualized, indicating the position alternation. The winding of the solid curves represents the swirling motion. The lowest level fluid, namely the red curve, endures strong spiral activity, while less for the higher ones, namely the solid blue and black curves. However no spiral motion can be observed for the dashed streamlines. And once they are entrained into the near wall region, their positions remain.

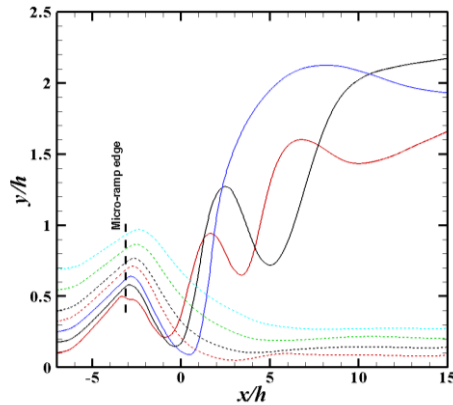


Fig. 16. The projected streamline in the x - y plane, the streamlines are those in figure 15(a).

Streamwise and wall-normal velocity components along the streamlines in figure 16 are further plotted in figure 17. Upon leaving the micro-ramp, a sudden drop of u is endured by the lower level flow due to the flow separation. Fluctuations are further experienced through the swirling in the deficit region and eventually recover to a higher magnitude, which is consistent with the recovery of momentum deficit.

A rapid increase of v can be observed close to the trailing edge, and a maximum is later reached. This is a common event for the fluid along these streamtraces and explains the focused upwash behind the micro-ramp. Similar to the behavior of u , fluctuating v is also exhibited. At far downstream, wall-normal velocity for all the streamlines approaches zero. The downward entrained flow with higher momentum, represented by the dashed curves, exhibits less fluctuation for both u and v , as no large scale vortical effects are present there.

At this point, the current observation does not give support to the prescribed knowledge of the working principle which considers the higher momentum in the downstream flow is entrained from the surrounding free stream. Because the foregoing illustrations find that the desired high momentum in the near wall region is achieved through the position alternation triggered by the micro-ramp instead of the downstream trailing vortex filaments.

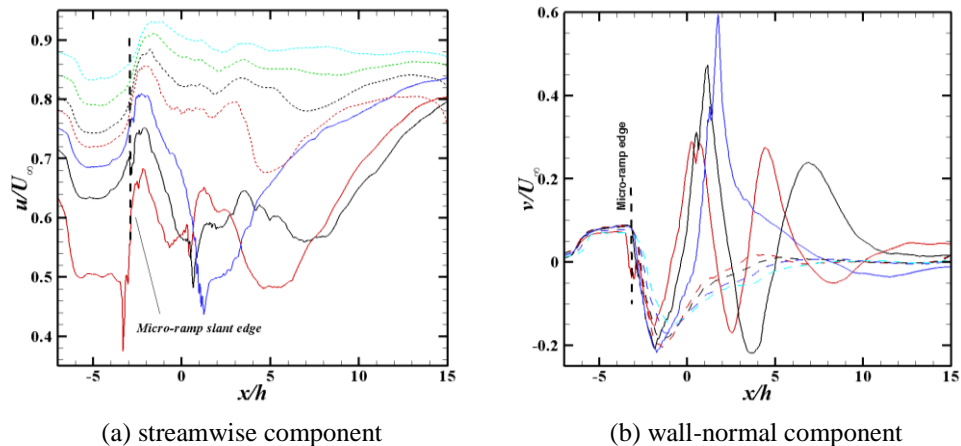


Fig. 17. The streamwise and wall-normal velocity components along the extracted streamlines.

8. Discussions and Conclusions

Throughout the above discussions, the implicitly implemented LES has been demonstrated to be capable of resolving the detailed structures in the supersonic micro-ramp flow, such as the primary vortex pair and the momentum deficit. The questions raised at the beginning of current research regarding the origin of momentum deficit and the relation between these two prominent structures can be answered and a revised mechanism of the micro-ramp can be updated:

- (1) The momentum deficit originates from the fluid in the lower portion of the incoming boundary layer along the whole span of the micro-ramp;
- (2) The high momentum fluid in the near wall region behind the micro-ramp is from the higher portion of the upstream boundary;
- (3) The downstream primary vortices are the remaining structures of the separated vortices at the slant edges. They are not capable of entraining free stream flow deep into the boundary layer.
- (4) The mechanism of the micro-ramp can so far be recognized as the position alternation of different portions of the incoming boundary layer, instead of being actuated by the downstream vortices.

Reference

- [1] J. C. Lin, Review of Research on low-profile vortex generators to control boundary-layer separation, *Progress in Aerospace Science* 38(4-5) (2002) 389-420.
- [2] S. Lee and E. Loth, Supersonic boundary-layer interactions with various micro-vortex generator geometries, *Aeronautical J.* 113 (1149) (2009) 683-697.
- [3] S. Lee, E. Loth and H. Babinsky, Normal shock boundary layer control with various vortex generator geometries, *AIAA paper* 2010-4254.
- [4] S. Lee, M. K. Goettke, E. Loth, J. Tinapple and John Benek, Microramps upstream of an Oblique-Shock/Boundary-Layer Interaction, *AIAA J.* 48 (1) (2010) 104-118.
- [5] H. Holden and H. Babinsky, Effect of microvortex generators on separated normal shock/boundary layer interactions, *J. Aircraft* 44 (1) (2007) 170-174.
- [6] H. Babinsky, Y. Li and C. W. PittFord, Microramp control of supersonic oblique shock-wave/boundary-layer interactions, *AIAA J.* 47 (3) (2009) 668-675.
- [7] M. Rybalko, H. Babinsky and E. Loth, VGs for a normal SBLI with a downstream diffuser, *AIAA paper* 2010-4464.
- [8] Q. Li and C. Liu, LES for supersonic ramp control flow using MVG at $M=2.5$ and $Re_0=1440$, *AIAA paper* 2010-592.
- [9] Q. Li, Y. Yan, P. Lu, A. Pierce, C. Liu and F. Lu, Numerical and experimental studies on the separation topology of the MVG controlled flow at $M=2.5$, *AIAA paper* 2011-72.

- [10] Y. Yan, Q. Li, C. Liu and F. Lu, Numerical, Experimental and Theoretical studies on the mechanism of K-H instability and ring generation behind supersonic MVG, AIAA paper 2011-676.
- [11] Y. Yan, C. Chen, X. Wang and C. Liu. LES study on the mechanism of vortex rings behind supersonic MVG with turbulent inflow, AIAA paper 2012-1093.
- [12] Y. Yan, Q. Li, C. Liu, A. Pierce, F. Lu and P. Lu, Numerical discovery and experimental confirmation of vortex ring generation by microramp vortex generator, Appl. Math. Modell. (2012), doi:10.1016/j.apm.2012.01.015.
- [13] W. R. Nolan and H. Babinsky, Characterization of the micro-vortex generators in supersonic flows, AIAA paper 2011-71.
- [14] Z. Sun, F. J. J. Schrijer, F. Scarano and B. W. van Oudheusden, The three dimensional flow organization in a supersonic boundary layer, Physics of Fluids, to appear.
- [15] C. Liu, L. Chen, Study of mechanism of ring-like vortex formation in late flow transition, AIAA paper 2010-4623.
- [16] Q. Li and C. Liu, Declining angle effects of the trailing edge of a microramp vortex generator, J Aircraft, 47(6) (2010) 2086-2095.
- [17] R. Giepman, personal communication.
- [18] J. M. Oorebeek, W. R. Nolan and H. Babinsky, Comparison of bleed and micro-vortex generator effects on supersonic boundary-layers, AIAA paper 2012-45.